GSA Data Repository item 2015302

Precambrian reidite discovered in shocked zircon from the Stac Fada impactite, Scotland

S.M. Reddy[1*], T.E. Johnson[1], S.Fischer[2], W.D.A. Rickard[3], and R.J.M. Taylor[1]

[1] *Department of Applied Geology, The Institute for Geoscience Research, Curtin University, GPO Box U1987, Perth, WA 6845, Australia*

[2] *Department of Earth and Environmental Sciences, University of St Andrews, St Andrews, Fife, KY16 9AL, UK*

[3] *Department of Imaging and Applied Physics, Curtin University, GPO Box U1987, Perth, WA 6845, Australia*

* Corresponding author: s.reddy@curtin.edu.au

Supplementary Sample Information and Detailed Methods

Sampled outcrops of the Stac Fada Member of the Stoer Group are exposed along the north side of the Bay of Stoer, Assynt, NW Scotland [NC 033 285]. The sample (14-SF-01), located at UK Grid Reference NC 03348 28515 (Latitude 58.2014, Longitude -5.3482), was taken from approximately 1.5 m above the base of a ~3 m thick unit that represents the lowermost Stac Fada unit of Young (2002). The sample is a matrix-supported, poorly-sorted breccia comprising centimeter-size clasts of lithic and devitrified melt fragments.

Zircon grains were separated using SelFrag high voltage pulse power fragmentation and heavy liquid separation at the Department of Applied Geology, Curtin University. Previous studies indicate that SelFrag does not lead to significant increases in the temperature or pressure of the separated phases and has no noticeable affect on zircon grains (Giese et al., 2010). Approximately 2kg of sample 14-SF-01 was loaded into a portable process vessel filled with de-ionized water. The base of the

process vessel was fitted with a 410 μm mesh. As the sample was progressively disaggregated, grains and fragments smaller than 410 μm fell through the mesh and into a collection vessel, which is isolated from further electrical pulses. Short pulses of high-voltage electrical fields were applied with a frequency of 2 Hz. Coarse fragmentation was achieved by applying five 140 kV pulses with an electrode gap of 40mm. The voltage was stepped down to 130 kV for an electrode gap of 30mm, and to 120 kV for an electrode gap of 20 mm. When the sample had been disaggregated into fragments of 10 mm or less, a voltage of 100 kV was applied for approximately 450 pulses, at which point the entire sample had passed through the 410 μm mesh.

The disaggregated sample was sieved using a 355 μm disposable mesh and the <355 μm fraction was placed in sodium polytungstate (NaPT) solution (specific gravity =2.85) and shaken vigorously to ensure that the full sample was suspended in the liquid. The grains were then allowed to settle for 3-4 hours. The material that sank was collected, thoroughly washed, and dried overnight at 50°C. Once dry, a hand magnet, was used to remove the magnetic fraction. The remainder was passed through a Franz magnetic separator with the magnetic fractions being drawn off in increments of 0.2 to 0.5 amps over a range of current settings from 0.1 to 1.7A. The non-magnetic (>1.7A) fraction was then hand-picked for zircon.

Approximately 200 separated zircon grains were mounted on an SEM stub and imaged using secondary electrons (SE) and backscattered electrons (BSE). The external morphology of one of the grains (grain #1) revealed planar lamellae ~2μm in width (Fig. DR1) that were subsequently identified as reidite. No other grains (including #86) showed lamellae on the external surface of the grain.

Following imaging, the grains were mounted in a 2.5 cm diameter epoxy disc and polished with 9 μm and 1 μm diamond paste. A final polishing with 0.06 μm colloidal

silica was done to remove surface damage. The polished mount was then coated with a ~3 nm layer of carbon to limit charging in the SEM and imaged using SE, BSE and cathodoluminescence. All SEM imaging and EBSD analysis was conducted on a Tescan MIRA3 Field Emission SEM, housed in the Microscopy & Microanalysis Facility (John de Laeter Centre) at Curtin University, Perth, Western Australia.

EBSD analysis involves the collection of electron backscatter diffraction patterns (EBSPs) from each node of a user-defined grid. The grid is defined by specifying the step size at which the electron beam is scanned over the surface of the sample. Each EBSP collected from the sample comprises a series of bands that represent the different lattice planes within the sample (Fig. DR2). The width of the band is related to the lattice spacing of that particular lattice plane and the different orientations of the bands in the EBSP represent the different orientations of the lattice planes. Areas in the EBSP where bands intersect are zone axes of the crystal lattice. The EBSP therefore records all the crystallographic information required to identify both the phase being analyzed (from lattice spacings) and crystallographic orientation (from band geometry) of the material with respect to the arbitrarily assigned sample coordinate framework.

To determine the phase and orientation of each EBSP, a process referred to as ‘indexing’, the empirically collected EBSP is compared to a database of theoretical diffraction patterns, commonly referred to as ‘match units’. In this indexing process the 8-10 strongest lattice planes in the empirically obtained pattern are matched by the acquisition software to the phases in the theoretical pattern database. During the acquisition process, an assessment of the quality of indexing is undertaken by calculating the mean angular deviation (MAD) between the empirical and theoretical patterns for the 8-10 bands used to index the EBSP. The MAD is a quantitative

measure of the robustness of the solution and a MAD of 1° was used as a filter such that for MAD > 1° a 'zero solution' was stored. In our analyses the MAD was typically ~0.5°. The crystal lattices of the three different Zr-bearing phases studied here are sufficiently different that indexing is able to easily discriminate between the different phases. Therefore by collecting our EBSD data at a resolution that is much smaller than the feature of interest (lamellae are typically 2μm and we used step sizes of 200nm, 50nm and 8nm), we are able to map the distribution of the different Zr-bearing phases within the zircon grains.

EBSD data were acquired using the automatic mapping capability of Oxford Instruments AZtec 2.3 software coupled with a NordlysNano EBSD detector. Match units used for indexing were derived from published crystallographic data for zircon (Hazen and Finger, 1979), reidite (Farnan et al., 2003) and baddeleyite (Gualtieri et al., 1996). Data acquisition and indexing ran at ~40 EBSPs per second. Full grain maps were collected at a step size of 200nm and for #1 and # 86 represent the analysis of ~730,000 and ~530,000 EBSPs respectively. Detailed maps represent 200,000 and 160,000 EBSPs for grains #1 and #86 respectively, and these were collected at a step size of 50nm. All EBSD data were post-processed using Oxford Instruments Channel 5.12 software to remove 'wildspikes' and interpolate non-indexed points using a 6 or 7 nearest neighbor filter following standard procedures (Reddy et al., 2007). The post-processed data files were then used to generate the presented EBSD maps.

EBSD maps of several types were used in this study. Band contrast is essentially an assessment of contrast between bands and background recorded in each empirically-derived EBSP. It is a measure of pattern quality and is a fundamental property of the EBSP. Band contrast is susceptible to variations in phase, crystallographic orientation, structural integrity, crystal damage and surface

topography and is therefore particularly useful for qualitatively delimiting the sample microstructure (e.g. Fig. 2). During data processing, band contrast maps were also used as a background over which phase or orientation data were draped. Phase maps were produced by assigning a different color to each identified phase. Orientation maps were produced using the Channel 5 'texture' component in which each pixel is colored for minimum misorientation relative to a user-defined reference orientation. Further details are given elsewhere (Reddy et al., 2007)

Crystallographic orientation data were plotted using Channel 5 "Mambo" software using lower hemisphere, equal area projections. All data are reported with respect to an arbitrarily assigned X-Y coordinate framework for the sample surface that is also shown in each of the orientation maps. Crystallographic axes of the zircon, reidite and baddeleyite were arbitrarily assigned specific miller indices in the sample reference frame to facilitate description and interpretation of the data.

The orientation of the lamellae in three dimensions was constrained in grain #1 from observation of lamellae in areas of the grain where zircon fragments had been plucked during the polishing process (Fig. 3). Zircon – reidite crystallographic relationships in grain #1 are shown in Fig. DR3.

To assess the orientation of the lamellae in grain #86, we used a Zeiss Neon 40EsB focused ion beam scanning electron microscope (FIB-SEM) housed at Curtin University to cut a section perpendicular to the polished surface of the grain (Fig. DR4a). An 8 nA, 30 kV Ga^+ ion beam was used for course milling, after which progressively lower current ion beams were employed for final polishing. The resulting thin foil (~100 nm thick) was removed from the grain using a nanomanipulator and mounted on a copper grid with platinum using ion beam deposition. Transmission Kikuchi diffraction (often referred to as transmission-EBSD

or t-EBSD) was conducted on the foil at a working distance level with the top of the EBSD detector and oriented perpendicular to a 30 kV electron beam. A step size of 8nm was used for the analysis. Data were noise reduced using the same settings as the EBSD surface data. The data from the foil were used to create an orientation map (Fig. DR4b). The orientation of the lamellae on the foil surface were used, with information from surface EBSD maps, to constrain the 3D geometry of the three lamellae orientations within grain #86. These orientation data (Fig. DR5) demonstrate that the interphase boundaries between zircon and reidite do not follow a systematic and rationale crystallographic relationship associated with martensitic shearing along the {100} planes in zircon (Fig. DR3 and Fig. DR5).

References Cited

Farnan, I., Balan, E., Pickard, C. J., and Mauri, F., 2003, The effects of radiation on local structure in the crystalline fraction of $ZrSiO_4$: Investigating the 29Si NMR response to pressure in zircon and reidite: American Mineralogist, v. 88, p. 1663-1667.

Giese, J., Seward, D., Stuart, F. M., Wüthrich, E., Gnos, E., Kurz, D., Eggenberger, U., and Schreurs, G., 2010, Electrodynamic Disaggregation: Does it Affect Apatite Fission-Track and (U-Th)/He Analyses?: Geostandards and Geoanalytical Research, v. 34, p. 39-48.

Gualtieri, A., Norby, P., Hanson, J., and Hriljac, J., 1996, Rietveld refinement using synchrotron X-ray powder diffraction data collected in transmission geometry using an imaging-plate detector: Application to Standard m-ZrO_2: Journal of Applied Crystallography, v. 29, p. 707-713.

Hazen, R. M., and Finger, L. W., 1979, Crystal structure and compressibility of zircon at high pressure: American Mineralogist, v. 64, p. 196-201.

Leroux, H., Reimold, W. U., Koeberl, C., Hornemann, U., and Doukhan, J. C., 1999, Experimental shock deformation in zircon: A transmission electron microscopic study: Earth and Planetary Science Letters, v. 169, p. 291-301.

Reddy, S. M., Timms, N. E., Pantleon, W., and Trimby, P., 2007, Quantitative characterization of plastic deformation of zircon and geological implications: Contributions to Mineralogy and Petrology, v. 153, p. 625-645.

Young, G. M., 2002, Stratigraphy and geochemistry of volcanic mass flows in the Stac Fada Member of the Stoer Group, Torridonian, NW Scotland: Transactions of the Royal Society of Edinburgh, Earth Sciences, v. 93, p. 1-16.

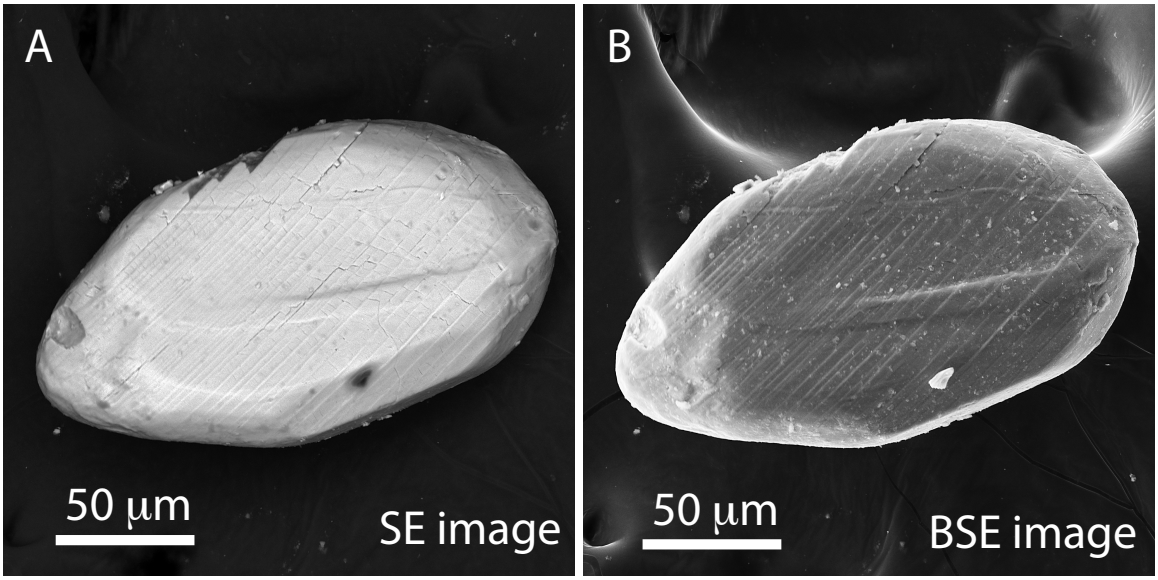

Fig. DR1. Secondary electron (A) and backscatter electron (B) images of grain 1 external morphology following mounting on carbon tape. A single set of planar lamellae, ~2um in width can be clearly seen transecting the zircon grain.

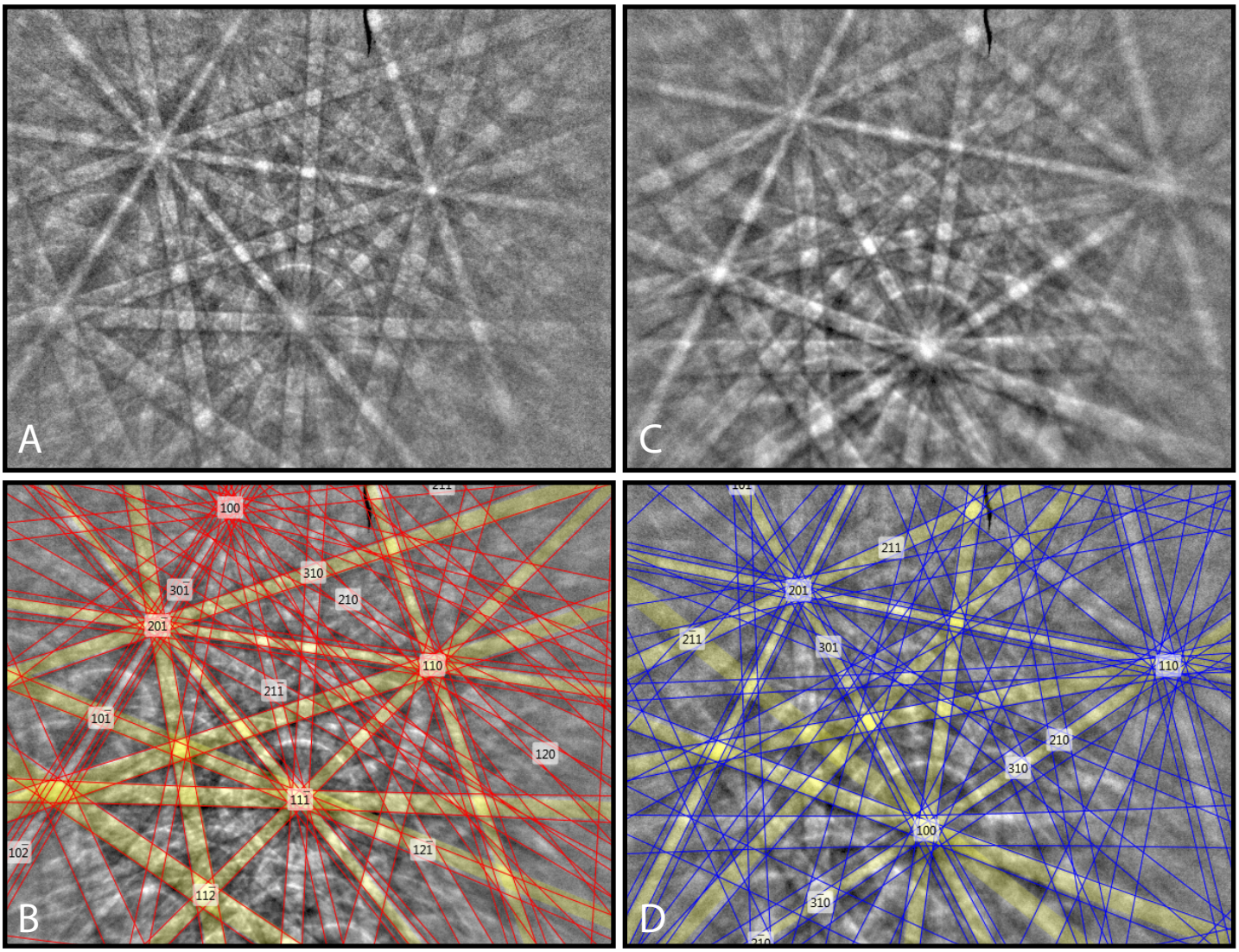

Fig. DR2. Electron backscatter diffraction patterns of a point within the host zircon and an adjacent reidite lamellae from grain #1. a) zircon EBSP. b) Zircon EBSP showing bands used to index the grain (in yellow) and the best fit indexing solution (red lines). c) Reidite EBSP. d) Reidite EBSP showing bands used to index the grain (in yellow) and the best fit indexing solution (blue lines). Numbers in b and d represent zone axes in Miller notation. In both cases number of bands used for indexing is 10 and mean angular deviation was <0.5°

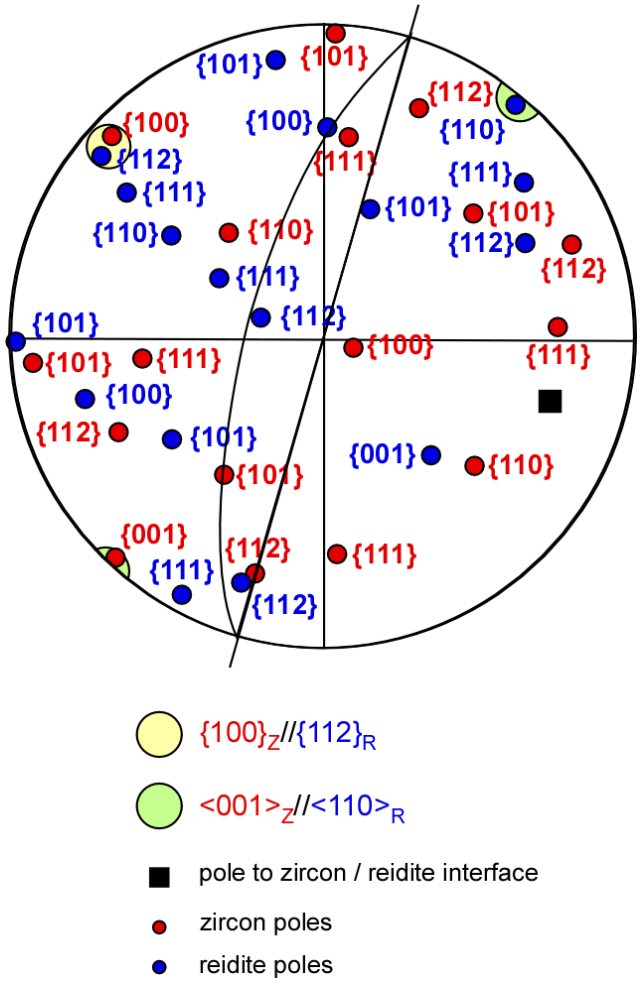

Fig. DR3. Lower hemisphere, equal area pole figures of zircon and reidite relationships in grain 1. Straight black line shows the trend of the trace of the lamellae. The 3D orientation of the lamellae are inferred from an area where sample has been plucked from the margin of the grain (see Fig 2a of published manuscript). The curved black great circle shows the approximate boundary between the zircon and reidite and it differs from the crystallographic coincident planes $\{100\}_{zircon}//\{112\}_{reidite}$ and directions $[001]_{zircon}//<110>_{reidite}$

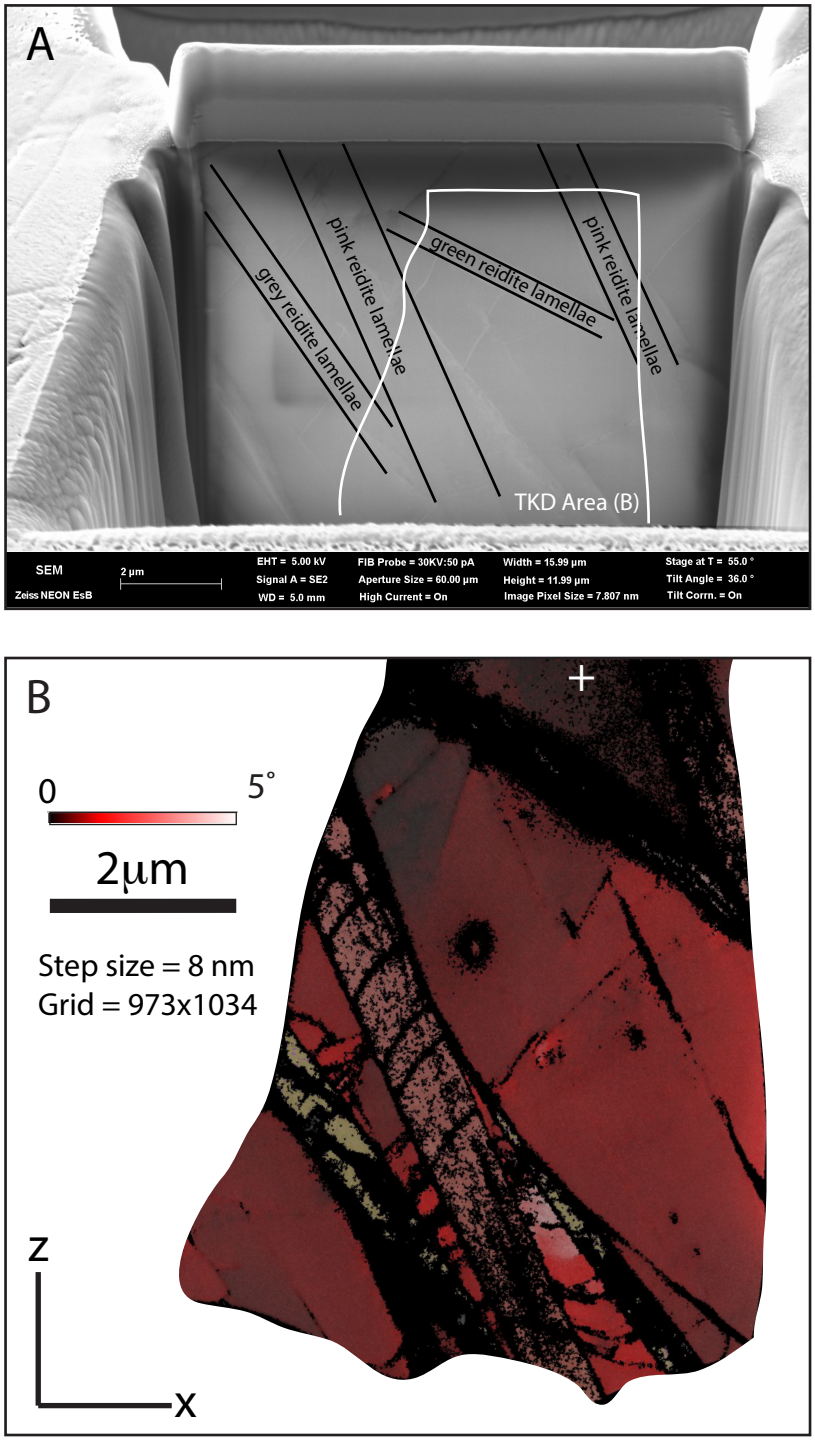

Fig. DR4. A. Secondary electron image of in-situ foil, prior to extraction, created by FIB milling of grain 86. Lamellae labels refer to colors shown in Fig. 3d of original manuscript. White line shows area of mapped foil shown in B. The pitch of the lamellae on the foil surface allows the 3D orientation of the lamellae to be constructed (see Fig. DR5). B. Transmission Kikuchi Diffraction orientation map of the thinned foil shown in A. Zircon is shown in red and is colored for orientation variations up to 5° from the white cross. Reidite lamellae are colored with respect to the inverse pole figure shown in Fig 3d. Substructure in reidite lamellae are zones of poor indexing that may represent amorphous material.

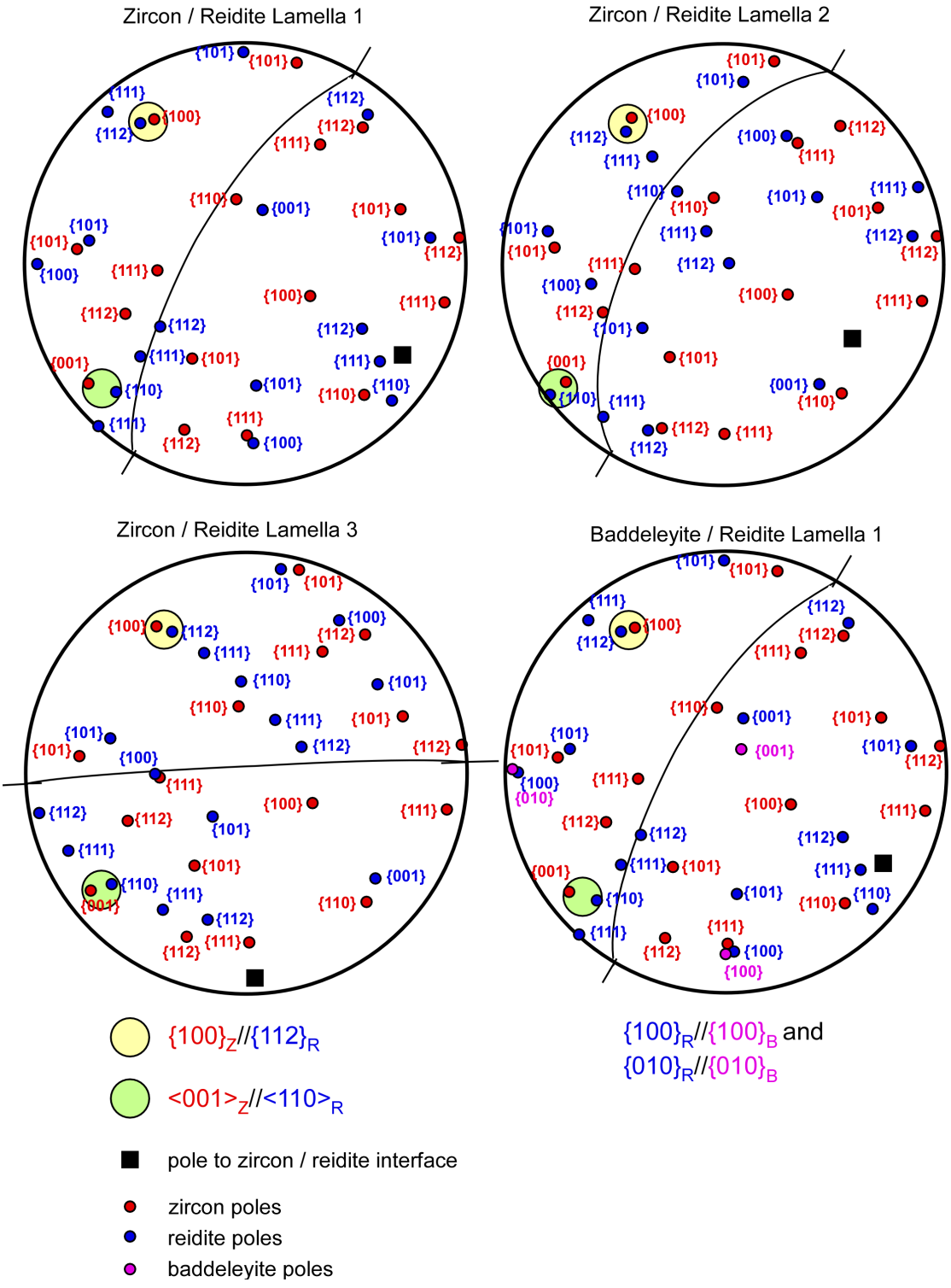
Zircon / Reidite Lamella 1
Zircon / Reidite Lamella 2
Zircon / Reidite Lamella 3
Baddeleyite / Reidite Lamella 1
{100}Z//{112}R
<001>Z//<110>R
{100}R//{100}B and
{010}R//{010}B
pole to zircon / reidite interface
zircon poles
reidite poles
baddeleyite poles

Fig. DR5. Lower hemisphere, equal area pole figures of zircon, reidite and baddeleyite relationships in grain #86. Poles are red = zircon, blue = reidite, purple = baddeleyite. Data are plotted for zircon relationships to the three different reidite lamellae in grain #86. In all cases there is coincidence of $\{100\}_{zircon}//\{112\}_{reidite}$ and $[001]_{zircon}//<110>_{reidite}$, which is consistent with TEM observations {Leroux et al., 1999). However, analysis of the 3D geometry of the zircon/reidite boundaries (black great circles with corresponding pole) perpendicular to the sample surface by FIB milling and TKD (Fig. DR4) indicates that the phase boundaries are not low-index rationale boundaries. The relationship between reidite lamellae 86 and baddeleyite contained within it is $\{100\}_{reidite}//\{100\}_{badd}$ and $\{010\}_{reidite}//\{010\}_{badd}$.